Universität Zürich[UZH]

Bachelor Thesis

Energy Calibration and Fiducial Volume Selection for the XENON1T Experiment in the Neutrinoless Double Beta Decay Regime

Student	Simon Buse
Professor	Prof. Dr. Laura Baudis
Assistant	Chiara Capelli
Topic	Data Analysis XENON1T

Spring Semester 2019

Particle Physics

Abstract

The thesis at hand describes the data analysis of two different studies related to the neutrinoless double beta decay search ($0\nu\beta\beta$) with the XENON1T experiment. The first analysis corrects the reconstructed energy for an observed depth dependence of the two detector specific parameters $g1$ and $g2$. The correction factors are found to linearly depend on the depth z and are probably due to imperfect field corrections. Additionally the energy resolution for the neutrinoless double beta regime ($\sim 2.5\,\mathrm{MeV}$) is computed to be $\frac{\sigma}{E} = 1.1 \pm 0.4\%$. The second investigation determines the fiducial volume which maximises the sensitivity for the case of no signal detection from the hypothetical decay. The sensitivity figure of merit $S \sim \sqrt{\frac{M}{B}}$, with the mass M and the background rate B, has been investigated for different volumes with real data from the XENON1T "science-run-1" with a live time of 164 days. The sensitivity parameter has been found to have its maximal value for a superellipsoidal shape with approximately 800 kg of liquid xenon which leads to an estimated half life sensitivity of $1.9 \cdot 10^{24}$ years at a confidence level of 90 % for XENON1T.

Contents

Chapter 1

Introduction

The document a hand describes the work that was done in form of a bachelor thesis with the experimental particle physics group of Prof. Dr. Laura Baudis at the University of Zurich.

Even though the XENON1T experiment is designed for the search of dark matter particles, it would be great if it would have multiple purposes and could produce results in related fields of research. Since there is a double beta decaying isotope in the xenon target the hypothetical neutrinoless double beta decay, which is connected to fundamental open questions regarding the nature of neutrinos, can be studied.

The first chapter introduces the physical problems of dark matter and the neutrinoless double beta decay for which answers are searched for with the XENON1T experiment. After generally introducing the concepts, two experiments (EXO-200 & KamLand-Zen) and the current best results in theses fields are disused.
The second chapter describes the energy calibration procedure and the energy resolution of the experiment. Furthermore, the depth dependence of the energy calibration and a resolution comparison to the previously introduced experiments is described.

In the third chapter the question of which volume inside the detector should be viewed as the target, for the search of the neutrinoless double beta decay, is answered.

The last chapter places the computed values for the XENON1T experiment into perspective to similar particle physics experiments and relates the obtained results.

Chapter 2

Physics with XENON1T

The following chapter introduces the reader to some of the current problems in particle and astroparticle physics and the attempt to resolve them with the XENON1T experiment.

2.1 Dark Matter

Conceptually the problem of dark matter is very similar to the old problem of unseen planets. By observing astrophysical systems some anomalies appear and theories explain them either by assuming the existence of a large amount of unseen mass or by assuming deviations from the known laws of gravity. The history showed that both solutions can be accurate and one of them usually solves the problem. In case of the orbital motion anomalies of Uranus the postulation of a unseen mass within the solar system lead to the discovery of Neptune and, in the case of Mercury's motion anomalies, Einstein's theory of gravity was required to correctly describe the orbit [1].

The issue today is that Einstein's field equations and the ordinary visible amount of matter in the universe are not sufficient to describe many astrophysical anomalies. Similar to the case of Uranus, multiple anomalies could be explained by proposing a large amount of matter that is not observable via electromagnetic interactions. This theory introduces what is referred as dark matter (DM) and is by far the most accepted solution. Below follows a list of observations which are in need of an explanation.

Rotational velocities in galaxies: If the orbital speeds of visible stars or gas in a disc galaxy is plotted against the radial distance from that galaxy's centre, one does not observe the expected $v \sim 1/\sqrt{r}$ relation which is predicted by the equality of the gravitational and the centrifugal forces and the observed mass distribution. Instead, flat rotation curves, see figure 2.1, are observed which can be explained by more unseen mass in the system [2].

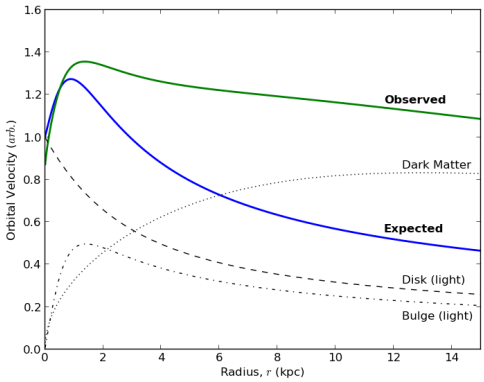

Figure 2.1: In blue the expected and in green the observed rotation curves. The observed rotation curves could be explained by adding a unseen mass distribution that causes an increasing rotation curve, indicated with the black dotted line. Figure from [3].

The bullet cluster: In the collision of two clusters of galaxies the visible matter and the gravitationally interacting matter are observed to be separated. The electromagnetically interacting gas, which makes up the most of the ordinary matter, is slowed down while the stars of the galaxies bypass each other almost undisturbed. Observations of the gas through X-Rays and gravitational lensing show a displacement between the visible mass and the gravitationally interacting mass, see figure 2.2 [4].

Figure 2.2: The gravitational lensing map (blue), overlayed over the optical and X-ray (pink) data of the Bullet cluster [5].

Structure formations: Without Dark Matter the universe would not have the observed structure. Since dark matter experiences no radiation pressure it clumps more efficient which forces the normal matter to form more dense structures as well. Simulations with no dark matter are not able to reproduce the observed large-scale structures [6].

Additionally to the astrophysical observations there are arguments coming from the cosmological ΛCDM model which points towards additional matter in the universe as well. The ΛCDM is very successful in explaining the temperature fluctuations in the cosmic

microwave background and predicts that the ordinary (baryonic) matter makes up to 15% of the matter in the universe and the missing 85% are dark matter [7].

The postulated dark matter has quite peculiar properties. For example, the term *dark* describes that it neither emits,absorbs or reflects light at any frequency. Maybe this non-interacting property would better be described with the term *transparent* matter. Secondly it is matter, it interacts gravitationally and the energy density falls off inversely with the volume. Thirdly it only interacts weakly both with itself and with other types of matter, where weakly means at least as weak as the weak interaction.

Generally the large scale behaviour of dark matter is much better understood than its microscopic properties. Dark matter seems to accumulate around galaxies, clusters of galaxies and form halos instead of being homogeneously spread through space.
These properties rule out all of the known particles in the Standard Model of particle physics as possible dark matter candidates. Even though the neutrinos would have very similar properties, they would be a candidate for what is called *hot dark matter*. This means that DM would be moving at a velocity comparable to the speed of light but this kind of behaviour is ruled out by many different reasons. For instance, the observed structure formations in the early universe would not have been possible with hot dark matter. Therefore dark matter must be cold which is to say non relativistic at the time of decoupling.[1]

One of the most popular class of candidates for dark matter are the WIMPs, which stands for *weakly interacting massive particles*. As the name suggests, they are relatively heavy (from a few GeV up to 10 TeV) and are predicted in different theories such as *neutralinos* which are introduced in supersymmetric theories. So far, there are three possible detection ideas.

- **Production:** If the dark matter particles are light enough they could be produced in high-energy collisions at the LHC. Since the DM needs to be stable it would carry away energy and momentum and would have a similar missing energy signature to the neutrino.
- **Indirect detection:** Through observation of visible decay products from dark matter particle-antiparticle annihilation one could find it indirectly. This method depends heavily on the dark matter density, astrophysical uncertainties and background sources.
- **Direct detection:** In an interaction with ordinary matter kinetic energy would be transferred to the atomic nuclei and the recoil energy (of the order of keV) could be detected. This requires shielding and rejection of backgrounds from ambient radiation. This is the method used by researchers in the XENON collaboration to detect the dark matter particles.

[1]The abbreviation CDM stands for *cold dark matter* and expresses exactly this feature.

2.2 The XENON1T Detector

The attempt to measure something as weakly interacting as the WIMP requires an environment with extremely low sources of background. Hence the XENON1T experiment is located deep underground in the *Labroratori Nazionali del Gran Sasso (LNGS)* in Italy. The 1.4 kilometers of solid rock above the laboratory have a 3.6 km water equivalent path length and shield effectively against cosmic rays and partially against atmospheric muons. The heart of the experiment, a xenon dual phase time projection chamber (TPC), is placed in a 10 m high water tank which is equipped with an active muon veto system. Additionally the water tank shields from the natural sources of radioactivity, such as the radon (^{222}Rn) originated from the naturally abundant uranium in the rocks. To further ensure low radioactivity, the XENON1T experiment is constructed of specially selected, screened and cleaned materials [8].

Time Projection Chamber

The XENON1T detector consists of a tank partially filled with gaseous and liquid xenon and a 248 light sensitive photomultiplier tubes watching its interior. The purified xenon needs to be cooled to about -90°C in order to be in the liquid phase. The very sensitive photomultiplier tubes (PMTs) monitor closely what is happening within the tank and pick up what ever light above the threshold (0.3 photoelectrons).

The idea is to measure an interaction of dark matter with ordinary matter as a scattering process of a xenon atom in the liquid phase. In such a particle collision the incoming particle transfers some kinetic energy to the xenon nucleus or an atomic electron surrounding the nucleus. The recoiling nucleus or electron, as it moves trough the liquid xenon, creates a track of excited xenon atoms $Xe^{\star}$, xenon ions Xe^{+} and free electrons e^{-}. This process is shown in figure 2.3 part 1a). The excited xenon atoms $Xe^{\star}$ de-excite by emitting scintillation light ($\sim 178\,\mathrm{nm}$) and create what is called the S1 light signal. This marks the first part of every detected particle collision. In the second part the freed electrons are drifted away from the place of interaction towards the top due to an electric field. At the liquid to gas interface there is a second electric field which allows one to extract the electrons into the gaseous phase and create a second light signal which is called S2, the proportional scintillation. The place of interaction can be derived from the light distribution in the PMT arrays, giving the x, y coordinates, while the depth z can be computed from time difference between the S1 and the S2 signal with the known drift velocity.

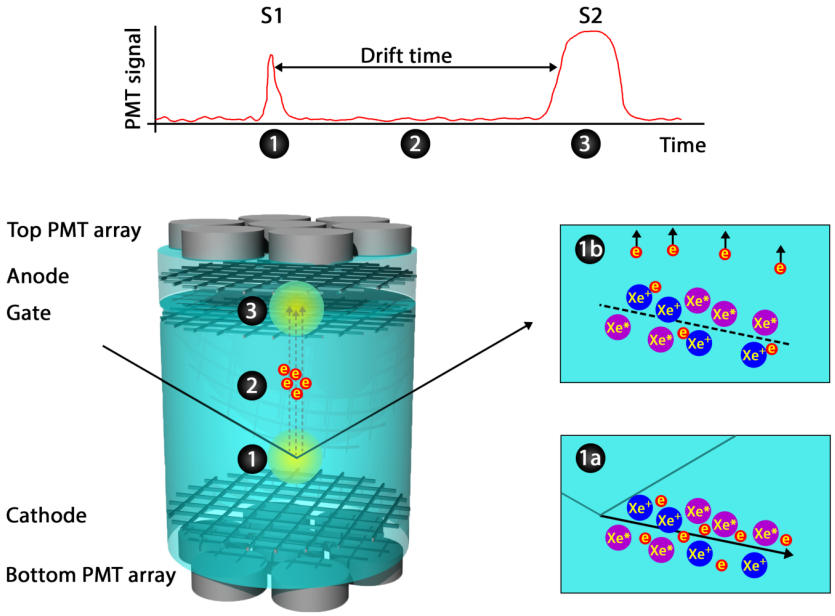

Figure 2.3: (Left): The operational principle of the XENON1T dual phase time projection chamber (TPC). The TPC is approximately 1 m high and has a diameter of 1 m. At the top a typical PMT signal is shown. (Right): 1a) the ionization and excitation of the xenon atoms due to a recoiling nucleus or an electron. (Right): 1b) The electrons drifting away from the place of interaction due to an electric field. Illustration taken from [9].

The S1 and S2 signal are not independent of each other and are linked through a process called *recombination*. Some electrons will recombine with xenon ions instead of being drifted away and the formed excited xenon atoms contribute to the S1 signal instead of to the S2 signal. Therefore there is an anticorrelation between the S1 and S2 signal which is clearly visible in the S1-S2 parameter space [2]. Since the fraction of freed electrons contributing to either the S1 or S2 signal is different even for interactions caused by mono energetic sources, careful data analysis is required to identify the incoming particle and the type of interaction that creates the measured pattern.

What is meant with the type of interaction is weather a xenon nucleus or an electron were hit by an incoming particle. In case of the nucleus one speaks of a nuclear recoil (NR) and sources of such a signal are for example neutrons or the dark matter candidates, the WIMPs. If an atomic electron is playing the role of the target one speaks of electronic recoil (ER) and the causing particles can be γ-rays or electrons from β-decays.

A crucial feature of the TPC is the possibility to differentiate events through the S2/S1 ratio and the number of S2 signals. With this an efficient background discrimination can be achieved. For example, more than one S2 signal is characteristic for a particle that

[2] See figure 3.1 at page 20 for an example.

scattered multiple times in the TPC, such as a neutron [8].

Why Xenon?

The reasons why xenon is used as a target material are diverse. Xenon is the rarest non radioactive element on Earth and can only be found in the atmosphere. It is a heavy element with a mean atomic mass off 131.1 atomic mass units [3]. The resulting liquid density, which is roughly 3 times the one of water, enables the construction of a relatively small detector with a high mass. Due to the linear dependence of the stopping power on the absorber density, there is an effective self-shielding mechanism which creates a region of very low background in the innermost part of the detector. The excellent scintillation properties and the relatively high boiling point add what is necessary to make an experiment technically feasible. The scintillation light of xenon is around 178 nm, which is directly detectable with special UV-sensitive PMTs [8].

2.3 XENON1T Dark Matter Search

Even though there are multiple things that can be investigated with the XENON1T detector, its main purpose is the search of the WIMPs. In September 2018 the collaboration published the results in which they analysed data from a 1 ton · year exposure. After an extensive analysis no excess of signal like events was found and with it the most stringent limits on the WIMP-nucleon spin-independent elastic scattering cross-section were set. For masses above $6\,GeV/c^2$, with a minimum of $4.1 \cdot 10^{-47}\,cm^2$ at $30\,GeV/c^2$ and 90 % confidence level, a large parameter space can be excluded, see figure 2.4 [10]. In order to get a feeling for the magnitude of the found limits a few examples of typical cross-sections are given in the table 2.1.

Process	σ
Neutron capture	$\sim 10^{-24}[cm^2]$ [11]
Thomson scattering	$\sim 10^{-25}[cm^2]$ [11]
DIS neutrino-nucleon scattering	$\sim 10^{-36}[cm^2]$ [12]
WIMP-nucleon scattering	$\leq 10^{-46}[cm^2]$ [10]

Table 2.1: Even tough cross-sections usually depend on s the center-of-mass energy and can vary greatly, the order of magnitude of a few different cross-sections are shown. They are ordered by the coupling strength of the mediating force, starting with the strong force followed by the electromagnetic and the weak force.

[3] $1a.u. = 1.66 \cdot 10^{-27}$ kg

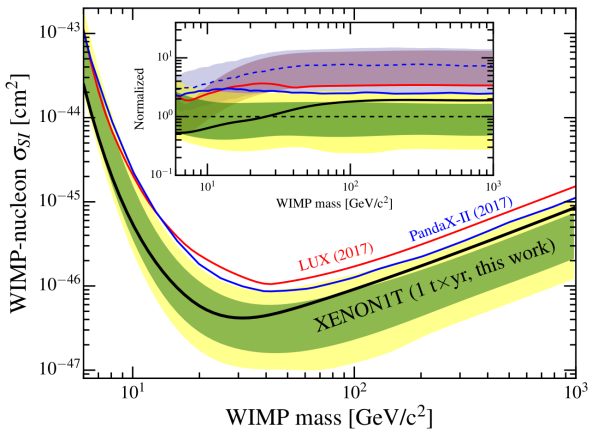

Figure 2.4: Results of the WIMP-nucleon spin-independent elastic scattering cross-section σ_{SI}. The thick black line shows the the upper limits of the 90% confidence level. In green and yellow the 1σ respectively 2σ sensitivity bands are shown. The inset shows the cross-section normalized to the median. [10]

Although the XENON1T detector was not able to solve the dark matter puzzle, it certainly proved its effectiveness for measuring rare processes by measuring the *two-neutrino double electron capture* of the ^{124}Xe isotope. The process that the XENON collaboration was able to measure in 2019 is the rarest ever directly measured decay. The half-life of $1.8 \cdot 10^{22}$ years exceed the age of the universe by 12 orders of magnitude [13]. [4]

2.4 The Neutrinoless Double Beta Decay of ^{136}Xe

Another interesting decay which can be looked for with the XENON1T experiment is the *neutrinoless double beta decay* ($0\nu\beta\beta$) which the ^{136}Xe isotope potentially could undertake. Unlike the also quite rare *two-neutrino double beta decay* ($2\nu\beta\beta$), the neutrinoless double beta decay is not allowed in the Standard Model of particle physics and is therefore a current research topic. Dedicated experiments usually work with enriched materials but the XENON1T detector, which was built for the detection of the WIMPs, has only 8.9% naturally abundant ^{136}Xe isotopes in it [5].

Similarly to the unseen planets and the dark matter problem it seems like history is repeating itself with the beta decays. In the 1930 *the missing energy problem* in the single beta decay imposed a great challenge on the physicists and lead ultimately to the postulation and discovery of the neutrino. Nowadays it is this special double beta decay process which may reveals the nature of the neutrinos and brings clarity to the neutrino hierarchy problem.

[4] The age of the universe is about $1.4 \cdot 10^{10}$ years according to the ΛCDM model.
[5] The naturally abundant $8 \cdot 10^{26}$ ^{136}Xe atoms amount to 178 kg of the 2 ton active detector mass.

The foundation to the $0\nu\beta\beta$ decay was introduced in 1937 by Ettore Majorana. He presented a new theory on how fermions could be described in a relativistic quantum field theory, which he thought to be especially useful for neutral particles. In Majorana's theory, the fields of the particle and the antiparticle coincide, as in the case for the photon. This behaviour is completely different to the known Dirac particles, the quarks and the charged leptons [14].

The simplest and the most appealing Feynman diagram with an exchange of a virtual massive Majorana neutrino ν_M is shown in figure 2.5. Instead of two electrons and two anti-neutrinos created in the normal double beta decay, there are only two electrons emitted which clearly violates the empirically motivated lepton number conservation.

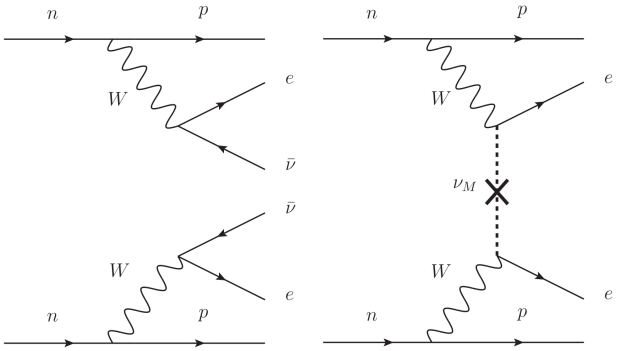

Figure 2.5: Feynman diagrams for the $2\nu\beta\beta$ decay (left) and for the not yet observed $0\nu\beta\beta$ (right).

The theoretical half-life $T^{0\nu}_{1/2}$ of the process is computed as follows:

$$(T^{0\nu}_{1/2})^{-1} = G^{0\nu}(Q, Z) \cdot |M^{0\nu}|^2 \cdot \langle m_{\beta\beta} \rangle^2 \tag{2.1}$$

with $G^{0\nu}(Q, Z)$ the phase space factor, $M^{0\nu}$ the nuclear matrix element between initial and final state and $\langle m_{\beta\beta} \rangle$ the effective Majorana mass term. The effective Majorana mass term $\langle m_{\beta\beta} \rangle$ is the coherent superposition of the three known light neutrinos.

$$\langle m_{\beta\beta} \rangle^2 = |\sum_{i=1}^{3} |U_{ei}|^2 e^{i\alpha_i} m_i|^2 \tag{2.2}$$

with m_i the masses of the three light neutrinos, U_{ei} the electron-elements of the PMNS-matrix and α_i the Majorana phases which are allowed in the Standard Model Lagrangian. If not observed, by measuring a lower limit of the half-life $T^{0\nu}_{1/2}$ of the decay, one can set a constraint on the effective Majorana mass term.

$$\langle m_{\beta\beta} \rangle \leq \frac{1}{\sqrt{T^{0\nu}_{1/2} G^{0\nu}(Q,Z)} |M^{0\nu}|} \tag{2.3}$$

Therefore studying the neutrinoless double beta decay sets constraints on the absolute neutrino mass scale and the Majorana phases in the PMNS matrix. Determining the nature of the neutrino, either Dirac or Majorana, would be a big milestone in completing the understanding of the elementary particles. A more complete explanation on how the Majorana neutrinos could be incorporated into the SM Lagragian and recent developments in the computation of the phase space factor $G^{0\nu}(Q,Z)$ and the nuclear matrix element $M^{0\nu}$ can be found in reference [14].

Experimental Signature

The reaction equation described in the right part of figure 2.5 would look as follows:

$$(A,Z) \rightarrow (A,Z+2) + 2e^{-}$$

In the decay two neutrons turn into two protons by sending of two electrons and increase Z by two. In principle a nucleus can decay as long as it becomes lighter trough the decay. If the nucleus can decay trough a single beta decay instead of two simultaneous beta decays, the decay through the single beta decay will be heavily favoured. Hence candidates for the $0\nu\beta\beta$ decay are isotopes where the single beta decay is kinematically forbidden since it would lead to a higher final state mass. The left illustration in figure 2.6 shows the mass function for the $0\nu\beta\beta$ candidates.

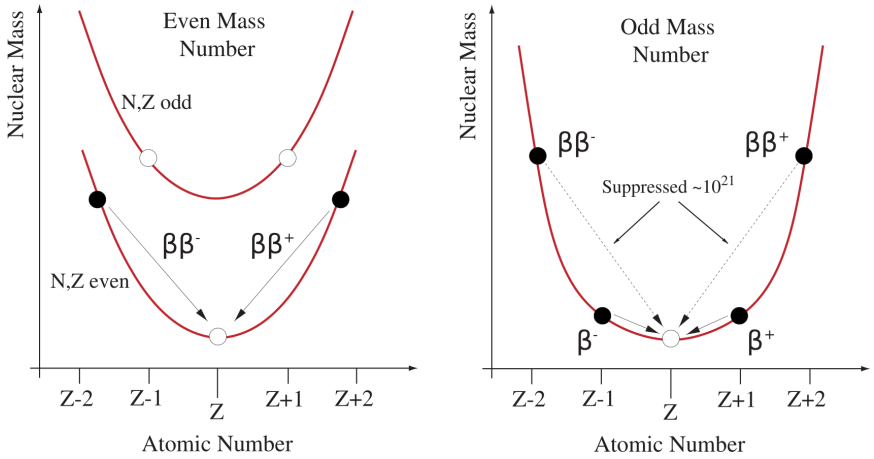

Figure 2.6: The nuclear mass as a function of the atomic number Z. Possible $0\nu\beta\beta$ candidates have to be of the even-even type (left). This type of nuclei are known to be more stable than odd-odd nuclei (right) due to the forbidden intermediate state [14].

In the $2\nu\beta\beta$ decay, the released energy is shared between the two electrons and the two neutrinos. This creates a continuous energy spectrum shown in figure 2.7. The total

amount of energy released in the decay is called Q-value and it is computed as the difference in the initial and final state mass: $Q = (m_i - m_f)c^2$

If there are no neutrinos produced in the decay and the electrons carry away the total change in binding energy, there should be a mono-energetic peak in the energy spectrum at exactly this Q-value. Due to the finite energy resolution a part of the $2\nu\beta\beta$ spectrum is actually giving a background signal to the $0\nu\beta\beta$ search. An excellent energy resolution is thus an important feature for a detector.

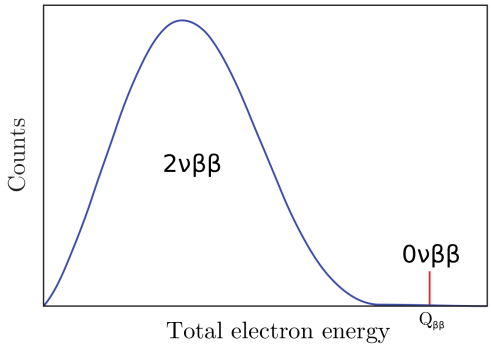

Figure 2.7: The continuous energy spectrum of the $2\nu\beta\beta$. Due to a final energy resolution it is one of the background sources for the measurement of the $0\nu\beta\beta$ decay. Of course the sharp line at the Q-value, $Q_{\beta\beta}$, would also be broadened through the detector resolution.

Currently the most precise results in this field of research are coming from Germanium-diode detectors, bolometers or from TPCs with enriched Xenon. Even though the energy resolution from the Xenon TPCs is nowhere near the ones of Germanium-diode detectors, the capability to reconstruct the event topology and the large exposure makes the XENON TPCs competitive [6]. Currently the best sensitivity, which can be interpreted as the process half-life that could be hidden by the background, suggests a half-life of the $0\nu\beta\beta$ decay greater than 10^{26} years [16]. This number should be compared to the before mentioned rarest ever directly measured process the *double electron capture* with a half-life of $1.8 \cdot 10^{22}$ years.

Two experiments which search for the neutrinoless double beta decay with the same isotope as the XENON1T experiment, are the EXO-200 in New Mexico and KamLAND-Zen in Japan. Both work with xenon enriched in the isotope ^{136}Xe and have concentrations of 80% and 90%, respectively.

[6] The relative resolution of GERDA is about 0.1% which is roughly a factor 10 times better than what will be presented in this work [15].

EXO-200

EXO-200 is a single phase TPC with a cylindrical geometry with approximately 40 cm diameter and 44 cm in length. The TPC provides an energy measurement and a spatial information of the ionization deposits by collecting the scintillation light and the charge, see figure 2.8(a). In contrast to the XENON1T experiment does the EXO-200 read out the created charge directly with a grid of wires instead of creating a second light signal in the gas phase. The wire technique allows a position accuracy of a few millimetres and an energy resolution around 1.5 %. Likewise as the XENON1T experiment, the EXO-200 is housed underground and has been constructed in a clean-room environment with specially screened and selected materials to ensure low radioactive background [17].

KamLAND-Zen

The current lowest limit for the $0\nu\beta\beta$ decay half-life $T^{0\nu}_{1/2}$ comes from the *KamLAND-Zen* experiment and suggests $T^{0\nu}_{1/2} \geq 1.07 \cdot 10^{26}$ years at 90 % confidence level. The original KamLAND oscillation experiment used one kiloton of liquid scintillator contained in a 6.5 m radius balloon to detect antineutrinos from Japan's nuclear reactors. KamLAND-Zen uses this large volume as an active shield for a central balloon with a diameter of 3 m which is filled with a xenon loaded liquid scintillator and contains approximately 300 kg of ^{136}Xe. The huge detector has 1879 PMTs installed which cover 34 % of the 4π solid angel. The success of KamLAND-Zen made clear that the large mass and the self-shielding can make up for the relatively poor energy resolution ($\approx$ 4.6 %) [16].

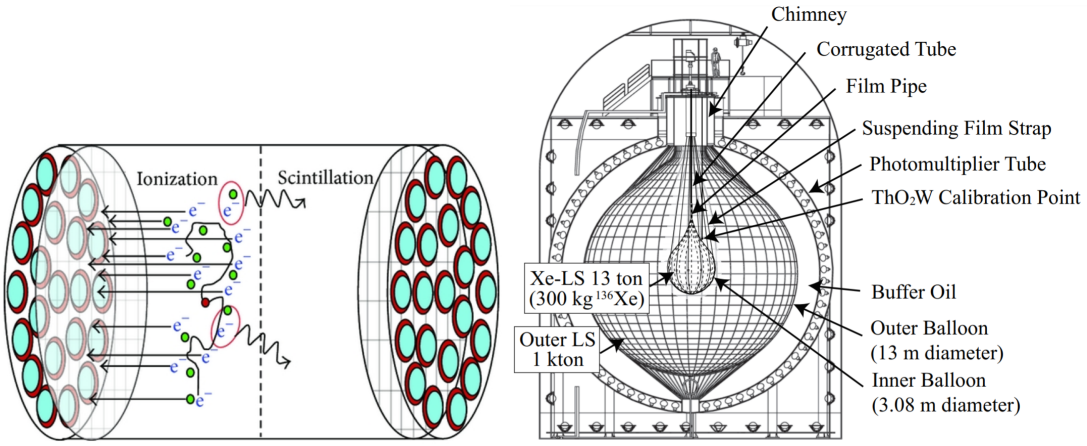

(a) The working principle of EXO-200 (b) The KamLAND-Zen experiment

Figure 2.8: In (a) the working principle of the EXO-200 experiment and in (b) the KamLAND-Zen experiment at the KamLAND facility. Figures from [17] [18].

Chapter 3

Energy Calibration

As mentioned in the introduction, the TPC allows for a detailed 3 dimensional event reconstruction. Additionally to the position reconstruction the recoil energy is one of the most important properties. In this chapter the calibration procedure for electronic recoils in the $0\nu\beta\beta$ regime (a few MeV) and the resulting resolution are being discussed. The analysis is performed on real data from XENON1T's *science-run-1* which lasted from February 2017 until February 2018. A detailed description of the used data can be found in the appendix 6.1.

3.1 Energy Reconstruction Procedure

By looking at an S1 vs S2 histogram, see figure 3.1, a few patterns are directly apparent. Firstly larger values of S1 and S2 reflect more intense light signals i.e. more photoelectrons [*pe*] and therefore larger energy of the incoming particle. Hence the more energetic events are found in the upper right corner and low energetic ones in the lower left corner. The signals in the upper right corner mark the end-point of the natural gamma radioactivity at an energy of 2.6 MeV caused by thallium 208. Signals which create even bigger S1 and S2 belong to α or β decaying elements and are not shown in this histogram.

Secondly there are clusters corresponding to mono energetic $\gamma-$lines with the mentioned anti-correlation between S1 and S2. The anti-correlation, manifested in a rotation angle of the clusters, is present due to the recombination mechanism [1] discussed in section 2.2.

Thirdly there is a gap in the upper right corner. In order to prevent a human bias, the data are blinded around the region where a signal of the ^{136}Xe $0\nu\beta\beta$ decay is expected. The idea is that the whole analysis should be done without knowing if there is a signal and when all the corrections and cuts are developed the region of interest can be unblinded.

[1] The recombination makes S1 a function of S2 and vice versa.

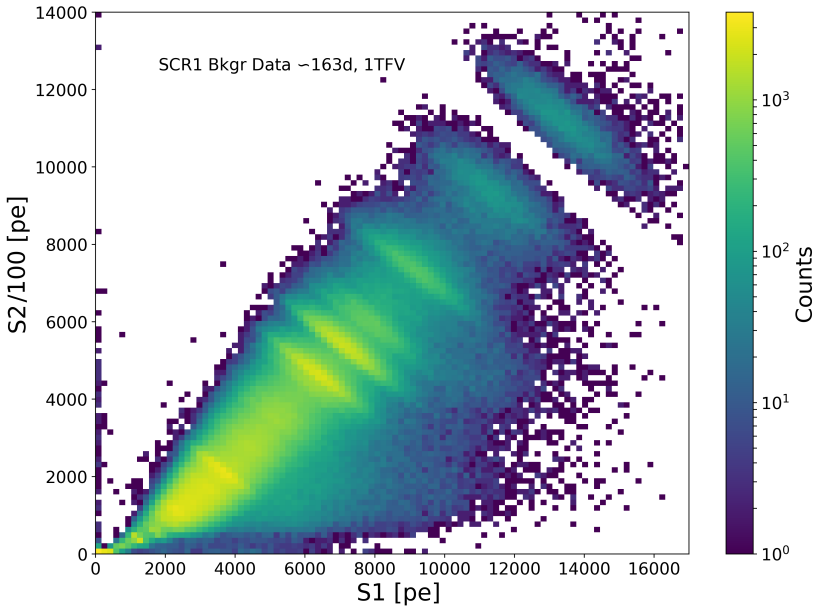

Figure 3.1: A histogram of S1 vs S2/100.

The histogram in figure 3.1 is generated from pure background data, there were none of the available calibration sources present during data taking. Since the WIMP and the $0\nu\beta\beta$ regions are blinded, the appearing clusters are only due to different sources of background for example decaying elements from the construction materials, intrinsic or activated sources within the liquid xenon.

It turns out that physics involved for electronic recoils is much simpler than for nuclear recoils and creating a single detectable quantum in liquid xenon takes a constant amount of energy $W = 13.7eV$ [19]. For ERs thus the original deposited energy E can be reconstructed through estimates of the detected number of photons n_{ph} and electrons n_e [20]:

$$E = W(n_{ph} + n_e) \tag{3.1}$$

Estimators for the number of photons n_{ph} and the number of electrons n_e are

$$n_{ph} = \frac{\mu_{S1}}{g1} \qquad n_e = \frac{\mu_{S2}}{g2} \tag{3.2}$$

with μ_{S1}, μ_{S2} the mean of S1 and S2 for a given energy deposition and $g1, g2$ two detector specific response factors which are to be determined .[2] Putting the estimators into

[2]Note that $g1, g2$ are detector specific factors which can depend on many different parameters and are not independent off each other.

equation 3.1 results in equation 3.3.

$$E = W\left(\frac{\mu_{S2}}{g1} + \frac{\mu_{S2}}{g2}\right) \tag{3.3}$$

The idea, illustrated in figure 3.2 (a), is that events from a monoenergetic decay accumulate around two mean values μ_{S1} / μ_{S2} which can be found by performing a two dimensional Gaussian fit. If the accumulation of events can be identified with a certain element, the energy E and the mean generated signals μ_{S1} and μ_{S2} can be found.

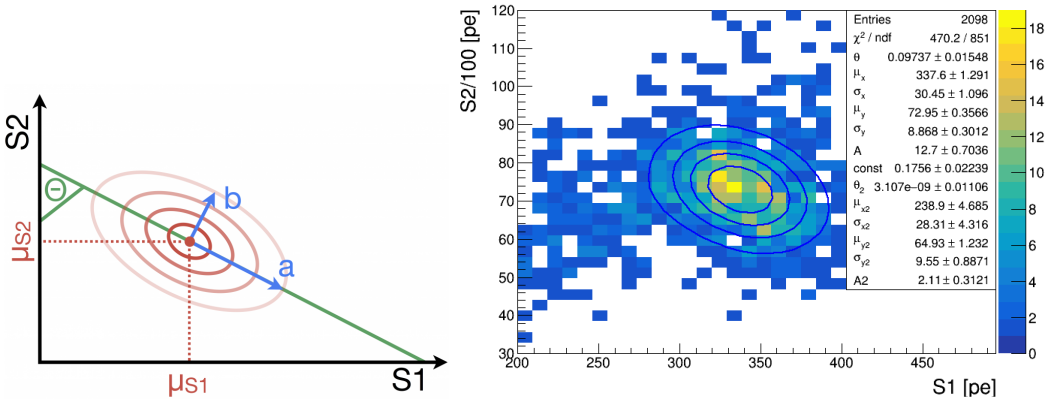

(a) 2D Gaussian fit method

(b) Fit example from krypton (Kr83m)

Figure 3.2: Fitting an accumulation of (S1,S2) data points with a 2D Gaussian distribution.

Equation 3.3 can be rewritten in order to display a linear relationship between the ratio $\frac{\mu_{S1}}{E} := QY$ called the *charge yield* and the ratio $\frac{\mu_{S2}}{E} := LY$ called the *light yield*.

$$\frac{\mu_{S2}}{E} = \frac{g2}{W} - \frac{g2}{g1}\frac{\mu_{S1}}{E} \quad \rightarrow \quad QY = \frac{g2}{W} - \frac{g2}{g1}LY \tag{3.4}$$

With multiple values of E, μ_{S1}, μ_{S2} a so called 'Doke' plot, which displays the anti correlation between QY and LY, can be created. The values $g1, g2$ can be computed from the slope and the y-axis intersection of a linear fit. With the knowledge of $g1$ and $g2$ the energy can be reconstructed by using the following formula:

$$E = W\left(\frac{S1}{g1} + \frac{S2}{g2}\right) \tag{3.5}$$

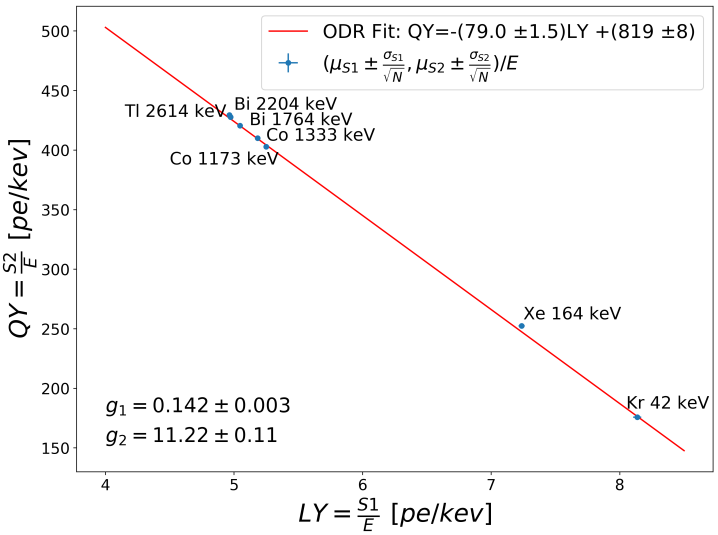

Figure 3.3: An example of a calibration 'Doke' plot. The errorbars $\pm\frac{\sigma_{S1}}{E\sqrt{N}}$ are drawn but are effectively suppressed by $\sqrt{N}$, the square root of the number of entries in each histogram. ODR refers to a fitting method called *orthogonal distance regression* and is described in the references [21],[22]. This method takes into account the uncertainty in both variables, the dependent and the independent variable, and has shown to produce better fit results as the *least-square method* which only considers an uncertainty in the dependent variable.

The described calibration method translates into the following steps:

1. Identify a cluster in the S1 vs S2 parameter space with a decaying element and the energy released in the decay.
2. Extrapolate the means μ_{S1} and μ_{S2} by performing a 2D Gaussian fit to the identified cluster in the histogram.
3. Use the means μ_{S1},μ_{S2} to create the calibration ('Doke') plot and perform a linear fit to find $g1$,$g2$ from the slope and the intercepting point.
4. Use $g1$,$g2$ and compute the energy for a given interaction from a measurement with formula 3.5.

3.2 Energy Resolution

The question on how precise the measurement is done can be answered by analysing spectral lines in the energy spectrum. An example of a full energy spectrum can be seen in figure 3.9 on page 26. The resolution is formally defined as [23]:

$$R = \frac{FWHM}{H_0} = C \cdot \frac{2.35\sigma}{E} = C1 \cdot \frac{\sqrt{E}}{E} = \frac{C1}{\sqrt{E}} \tag{3.6}$$

Where $FWHM = 2.35\sigma$ is the full width at half maximum of the energy peak and is proportional to $\sqrt{E}$. H_0 is the mean pulse height corresponding to the same peak and it is proportional to the energy E. To compute the resolution function the monoenergetic lines in the energy spectrum are fit with Gaussian functions and there resolution is defined as $R = \frac{\sigma}{E}$. Two examples of this fitting procedure can be seen in figure 3.4.

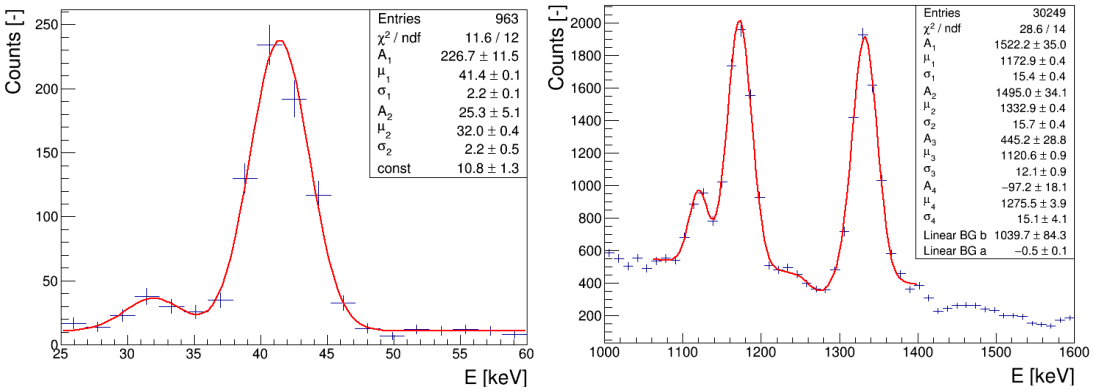

(a) Krypton (Kr83m) at 42 keV

(b) Cobalt (Co60) at 1.1 and 1.3 MeV

Figure 3.4: Energy histograms of the krypton and the two cobalt lines including a fit. The background shape next to the peaks have to guessed in order to find an appropriate width σ of the Gaussian peaks.

With the values from the fitting procedure the resolution plot can be generated, an example is shown in figure 3.5. Ideally the resolution, which expresses the ability to detect a very sharp line as such, would be extremely low. The resolution in figure 3.5 is low for large energies but increases significantly for low energies. The used fit function takes the following form, the constant C_0 is added in order to account for a minimal resolution [23]:

$$R = \frac{C_1}{\sqrt{E}} + C_0 \tag{3.7}$$

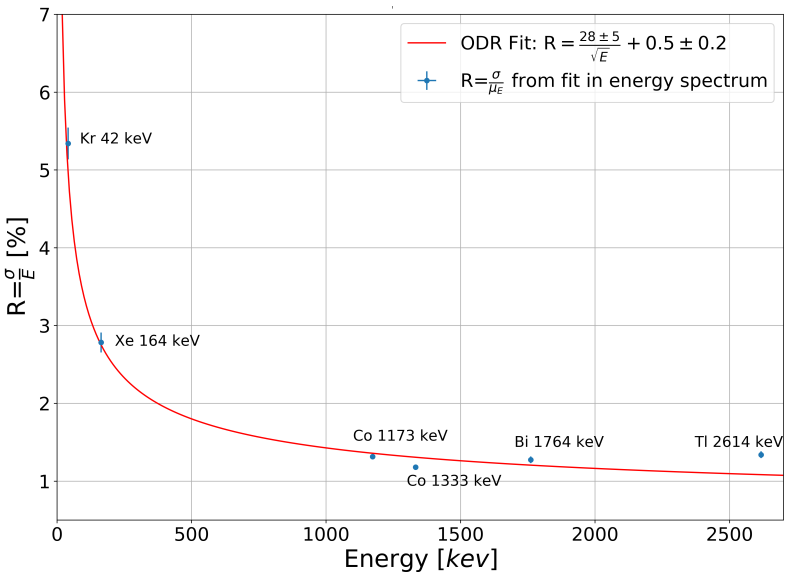

Figure 3.5: Resolution depending on the energy. The data points $R = \frac{\sigma}{\mu_E}$ are computed from Gaussian fits to monoenergetic lines in the energy spectrum and are then fitted with a function according to equation 3.7.

3.3 Depth Dependent Correction

After performing the energy calibration one can have a look at the two dimensional histogram in figure 3.6. It shows the energy of events happening in the TPC w.r.t the depth (z coordinate). It is apparent that all the lines get slightly shifted towards higher energies when the depth increases. This behaviour is presumably due to imperfect field corrections, $g1$ and $g2$ should in principle be independent of z. To account for shift of the spectral lines the two calibration factors $g1$ and $g2$ have to be corrected w.r.t the depth. From a previously done analysis this correction was found to be linear such that the combined energy formula changes as follows.

$$E = W\Big(\frac{S1}{g_1(z)} + \frac{S2}{g_2(z)}\Big) = W\Big(\frac{S1}{a_1 z + b_1} + \frac{S2}{a_2 z + b_2}\Big) \tag{3.8}$$

In order to find the z-dependence of $g1$ and $g2$, the idea is to slice a given dataset according to the depth and repeat the calibration procedure for each slice. The dataset described in appendix 6.1 was sliced into 5 different subsets such that each subset covers approximately 17 cm of height in the TPC. After running the described calibration procedure in all the slices the z-dependence, shown in figure 3.7, of the factors $g1$ and $g2$ was found.

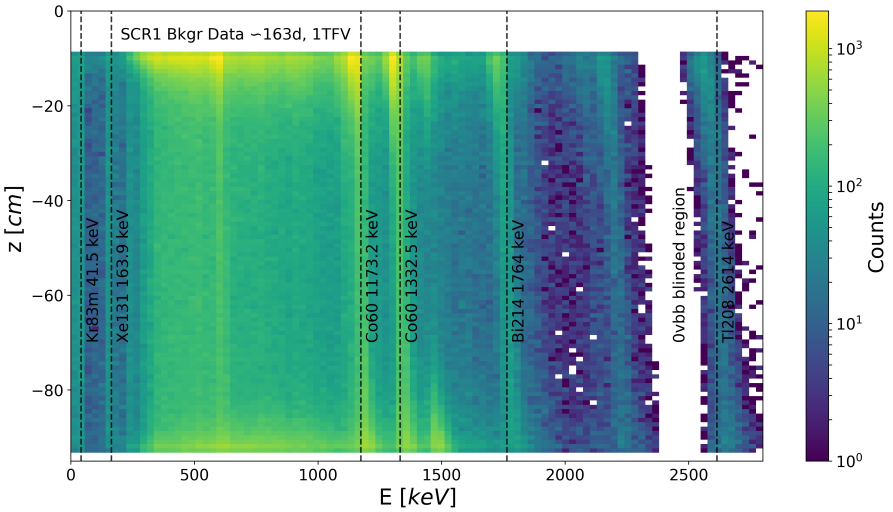

Figure 3.6: Energy vs depth histogram. The motivation for the z-correction comes from the shift of the spectral lines with increasing depth. The zero point in the z-coordinate is defined at the gate electrode.

3.4 Results

The described procedure revealed the following results for the function of $g1(z)$ and $g2(z)$.

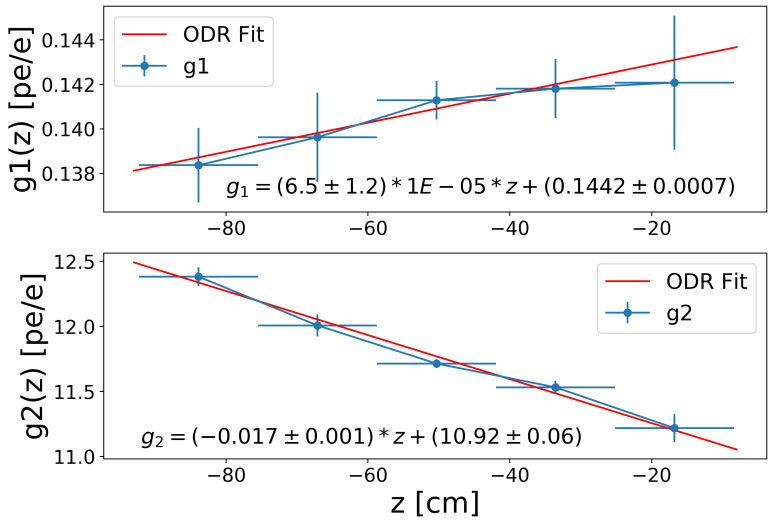

Figure 3.7: Fit to the different $g1$ and $g2$ at different depths. The uncertainty in the z coordinate is set as half the width of the slice thickness and taken into account trough the ODR fitting algorithm [22] [21].

The corrected values of $g1$ and $g2$ show an improved energy spectrum. The spectral lines in figure 3.8 appear sharper and increase the reconstruction precision.

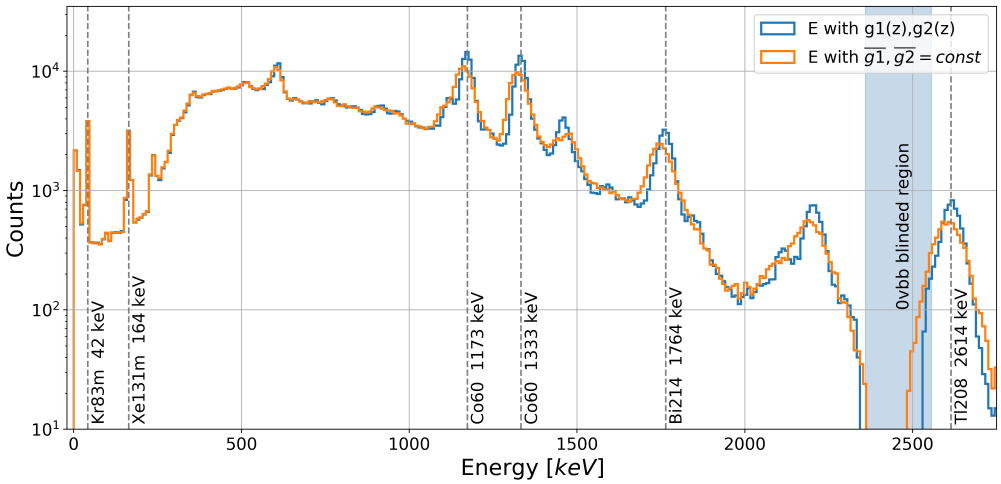

Figure 3.8: The energy spectrum including the z-correction is shown in blue and shown in orange is the spectrum with depth averaged values for g1 and g2.

The resulting resolution is shown in figure 3.9 which yields a relative resolution for the $0\nu\beta\beta$ decay of (1.1 ± 0.4) % [3].

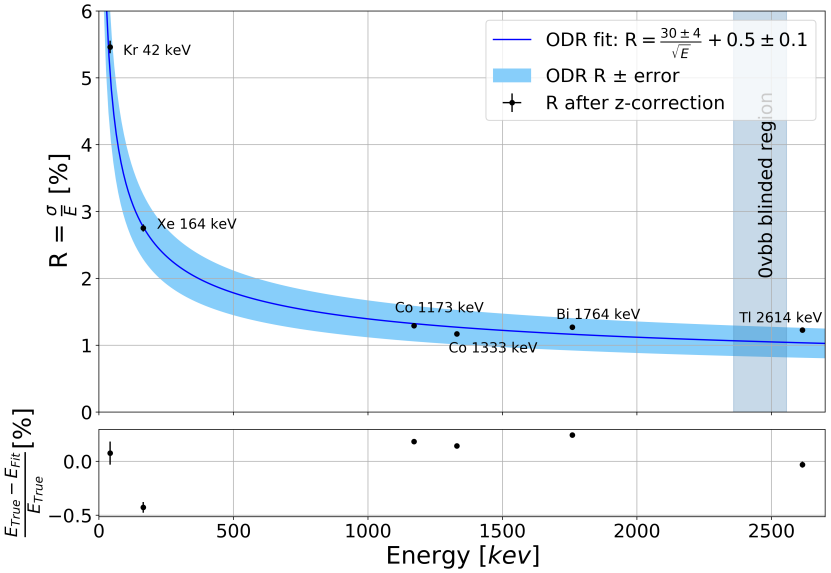

Figure 3.9: Resolution and energy shift from the true value with z-correction. The value E_{Fit} refers to the fit value in the energy spectrum. The error band is computed by adding the uncertainties for the upper bound and subtracting the uncertainties for the lower bound. The bottom panel shows the shift obtained by fitting the individual gamma lines in the energy spectrum with Gaussians and appropriate backgrounds.

[3] $Q_{\beta\beta} = 2457.83 \pm 0.6$ keV [24]

3.5 Discussion

The found z-correction and resolution are in agreement with what was previously done in the XENON collaboration. No fundamentally new information but a weaker z-dependence, compared to the definition which was used to define the blinded region, was found, see table 3.1. XENON1T has a good resolution in the region of interest compared to dedicated experiments which look for the $0\nu\beta\beta$ decay with the same isotope ^{136}Xe, see table 3.2. This is a surprising attribute considering that XENON1T was built for the detection of a signal in the keV range.

Used for the $0\nu\beta\beta$ blinded region [4]	Determined in this work
$g1(z) = 0.0001 \cdot z + 0.146$	$g1(z) = 6.5 \cdot 10^{-5} \cdot z + 0.144$
$g2(z) = -0.017 \cdot z + 10.6$	$g2(z) = -0.0017 \cdot z + 10.9$

Table 3.1: Comparison of the functions for $g1$ and $g2$.

Experiment	Isotope	Technique	ΔE $[keV]$ [5]	R $= \frac{\sigma}{E}$ [%]
XENON1T	^{136}Xe	TPC	63 ± 23	1.10%
EXO-200 [25]	^{136}Xe	TPC, enriched	71 ± 3	1.23%
KamLAND-Zen [16]	^{136}Xe	loaded liquid scintillator	268 ± 11	4.65%

Table 3.2: FWHM Resolution in comparison to other experiments. The value for XENON1T is derived from the found resolution function, see figure 3.9.

Generally the *goodness of fit* turns out to be crucial throughout this analysis. In the 1D and 2D Gaussian fits one has to guess appropriate backgrounds and approximate them with polynomials in order to receive good fit results [6]. Especially in the 2D fitting this estimation and its influence on the found values is not clear and certainly a source of a systematic uncertainty. A combination of the reduced Chi square $\chi^2/ndf \stackrel{!}{=} 1$ and a graphical inspection was used to obtain reasonable results. The convergence of the ROOT minimizer did not turn out to be a useful criterion, which is why one would certainly increase the reproducibility and precision if a strict convergence criteria and a specific ROOT (Migrad/Hesse/Minos) minimizer is used.

The bin size in all of the shown histograms had to be done in a sensible and reproducible way. As described in reference [26], there are multiple ways of choosing the bin size automatically. Either the *Scott* or the *Freedman Diaconis Estimator* were used in this analysis and in datasets with a clear Gaussian peak, the bin size was tested to have only a minor influence on the fit results.

[4] Blinded region = $\{ E(g1, g2) \mid E \in [0.96 \cdot Q_{\beta\beta}, 1.04 \cdot Q_{\beta\beta}] \}$

[5] ΔE = the absolute resolution at FWHM, $\Delta E = 2.35 \cdot R \cdot Q_{\beta\beta}$

[6] This analysis turned out to be an extensive fitting exercise. In total around 55 fits to individual background shapes had to be done.

Chapter 4

Fiducial Volume Selection

The following chapter describes the task of finding the fiducial volume for the $0\nu\beta\beta$ decay which maximises the sensitivity. The sensitivity, usually expressed in years, can be approximated by the figure of merit S according to equation 4.1 in case of no peak detection in an experiment [14]. S can be viewed as the process half-life of whose signal can be excluded by the experiment with a confidence level of 90 % in the null hypothesis of only background. The statistical inference would therefore exclude a signal that is actually there in only 10% of the cases. The experiments strong dependence on the energy resolution ΔE is illustrated in figure 4.1 and the terms in equation 4.1 are described in table 4.1.

$$S = ln(2) \cdot \frac{\varepsilon}{n_\sigma} \frac{\eta}{\mathcal{M}_A} \sqrt{\frac{M \cdot T}{B \cdot \Delta E}} \tag{4.1}$$

Symbol	Name	Units	Assumend value
ε	detection efficiency	$[-]$	90%
n_σ	confidence level	$[-]$	1.6 for the confidence level of 90%
η	isotopic abundance	$[-]$	8.49% for ^{136}Xe [1]
$\mathcal{M}_A$	atomic mass	$[kg]$	136 a.u[2] for ^{136}Xe
M	mass of the fiducial volume	$[kg]$	to be determined in this chapter
T	measuring time	$[days]$	163.7 days for the used dataset
ΔE	FWHM energy resolution	$[keV]$	63.5 keV [3]
B	normalized background rate	$[\frac{counts}{keV \cdot kg \cdot days}]$	to be determined in this chapter
S	sensitivity	$[days]$	to be determined in this chapter

Table 4.1: Legend for equation 4.1.

[1] This is the measured value for XENON1T, naturally abundant ^{136}Xe is to 8.86%.
[2] $1 a.u. = 1.66 \cdot 10^{-27}$ kg
[3] $\Delta E = 2.35 \cdot R \cdot Q_{\beta\beta}$ with the relative resolution $R = \frac{\sigma}{E}$ from chapter 3.

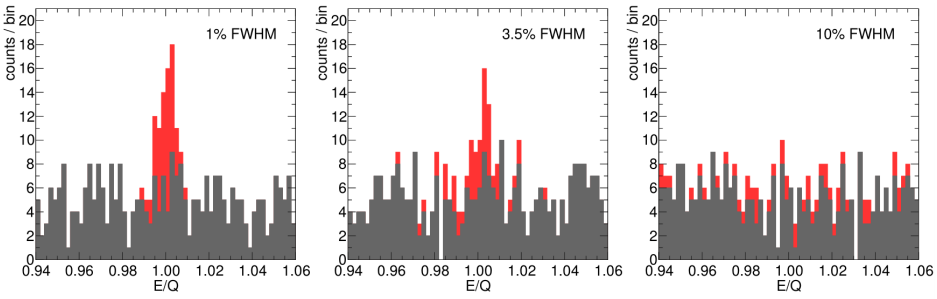

Figure 4.1: Signal and background (red and grey stacked histograms, respectively) in the region of interest around $Q_{0\nu\beta\beta}$ for 3 toy Monte-Carlo experiments with the same signal strength (50 counts) and background rate (1 $count \cdot keV^{-1}$), but different energy resolution: left: 1 % FWHM, center: 3.5 % FWHM, right: 10 % FWHM. The signal is distributed normally around $Q_{0\nu\beta\beta}$, while the background is assumed flat. Figure from reference [27].

The question at hand is, how to choose a volume inside the TPC which maximises this function. Among the factors in formula 4.1, only the background rate B and the mass M are influenced by the selection of a volume. This is translated into the relation $S \sim \sqrt{\frac{M}{B}}$. The background rate should be preferably very low[4], thus a small inner volume is preferred due to the self shielding of xenon, but the mass should be as large as possible. These two opposing trends ideally maximise the sensitivity for a selected volume inside the TPC. Since the TPC has a cylindrical shape, the most natural fiducial volume has the same symmetry. The so called *superellipsoid*, described by the following equation, is the perfect candidate for this symmetry:

$$\left(\frac{r}{r_{max}}\right)^t + \left(\frac{|z - z_0|}{z_{max}}\right)^t = 1 \quad with \quad r = \sqrt{x^2 + y^2} \tag{4.2}$$

There are 4 parameters which define the shape and the position of a superellipsoid. z_0 defines the coordinate origin and is fixed in this study to the center of the *1 tonne fiducial volume* [5], which was defined in the dark matter search to be at $z_0 = -51\,cm$. The remaining 3 parameters r_{max}, z_{max} and t define the maximal radial extension, the maximal height extension and shape of the superellipsoid respectively. The exponent t plays a very interesting role, namely it changes the shape, as it can be seen in figure 4.2 [6]. For $t = 2$ the superellipsoid is a regular ellipse revolved around the z-axis and with increasing t the shape becomes more and more cylindrical.

[4] Of course formula 4.1 is at one point no longer valid when the background B approaches zero.
[5] The 1T fiducial volume is defined as cylindrical volume with $r \in [-92.9, -9]\,cm$ and $z \in [0, 36.9]\,cm$
[6] In principle t can be chosen as any positive number but for $t \leq 1$ the shapes become concave which causes low masses.

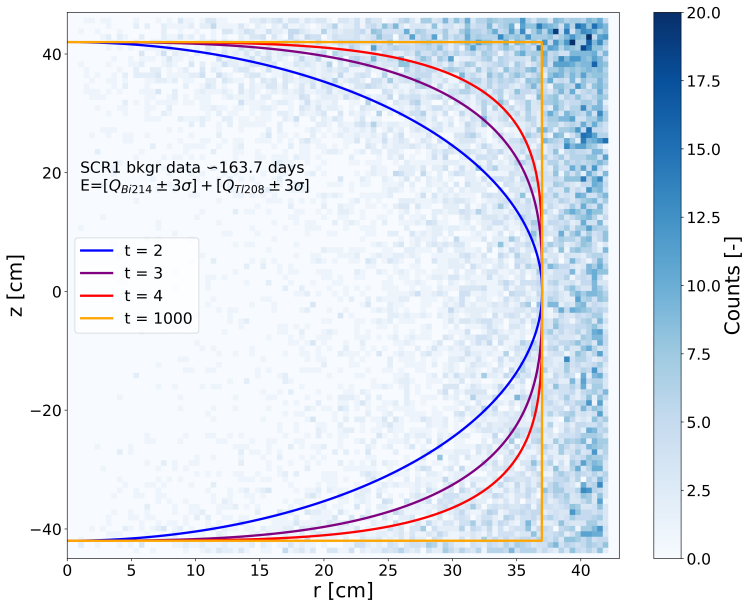

Figure 4.2: Superellipsoids with $z_{max} = 42\,\text{cm}$, $r_{max} = 37\,\text{cm}$ and different shape parameter t. Important to notice is the switch to cylindrical coordinates such that $z \in [-44, 44]\,\text{cm}$ instead of the usually used $z \in [-100, 0]$.

4.1 Optimization Problem

Finding the optimal radius r_{opt} , the optimal height z_{opt} and the optimal shape parameter t_{opt} can be described as a classical optimization problem.

$$r_{opt}, z_{opt}, t_{opt} = \underset{r_{max}, z_{max}, t}{argmax} \left\{ S \sim \sqrt{\frac{\rho \cdot V(r_{max}, z_{max}, t)}{B(r_{max}, z_{max}, t)}} \right\} \tag{4.3}$$

With the density of liquid xenon $\rho = 2.86 \frac{g}{cm^3}$ and V the volume of a superellipsoid given as [28]:

$$V(r_{max}, z_{max}, t) = \underbrace{\frac{4}{3t}\, \beta\left(\frac{1}{2}, \frac{1}{2}\right)\, \beta\left(\frac{2}{t}, \frac{1}{t}\right)}_{prefactor}\, r_{max}^2 \cdot z_{max} \tag{4.4}$$

Where β are the Euler beta functions which cause the *prefactor* $\in [\frac{4\pi}{3}, 2\pi]$ when $t \in [2, 1000]$, such that the usual formula for a cylinder holds at $t = 1000$.

4.2 Background Rate

The background rate B needs to be evaluated with a dataset. The final dataset depends on various cuts and preselections and a detailed description of the used dataset is given

in the appendix 6.1. Generally the rate is determined by simply counting the number of events within a given volume and then normalizing it to the energy range $[keV]$, the livetime $[days]$ and the mass $[kg]$ of the fiducial volume:

$$B(r_{max}, z_{max}, t) = \frac{1}{t[days] \cdot m[kg] \cdot E[keV]} \cdot \left\{ events | \left(\frac{r}{r_{max}}\right)^t + \left(\frac{z}{z_{max}}\right)^t \leq 1 \right\} \quad (4.5)$$

4.3 Energy Region

How to compute the sensitivity if no signal is detected is described by the formula 4.1 but this requires that the signal region around the Q-value is accessible which is not the case at the current status of the research. To be able to compute an estimation of the sensitivity which is well representing the analysis with unblinded data, an appropriate energy selection needs to be applied. It is important that the distribution of events in the TPC and the rate are as similar as possible to the actual measurement around the Q-value. Since the exact rate is not known, appropriate guesses had to be made and the choice fell on the two following energy regions for which the analysis was done separately. The two regions were selected because the two decay lines have a similar energy as Q-value and since another bismuth line at 2448 keV with a similar rate is expected within the blinded region:

Energy region 1: $E = [Q_{Bi214} \pm 3\sigma] + [Q_{Tl208} \pm 3\sigma]$

Energy region 2: $E = [Q_{Bi214} - 3\sigma, Q_{Tl208} + 3\sigma] - \underbrace{Q_{\beta\beta} \pm 4\sigma}_{blinded\ \ region}$

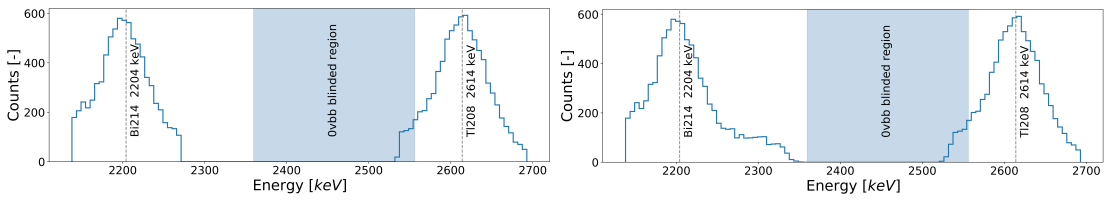

(a) Energy region 1 (b) Energy region 2

Figure 4.3: Energy spectra for the two selected energy regions. Notice that the blinded region seems ill-defined which is due to the use of different coefficients $g1, g2$ in the definition of the blinded region. The bismuth ^{214}Bi is due to the naturally accruing radon ^{222}Rn decay chain and is an intrinsic source whereas the thallium ^{208}Tl is present in the construction materials.

4.4 Results and Discussion

The evaluation of the sensitivity revealed contour plots like the one shown in figure 4.4 (a).

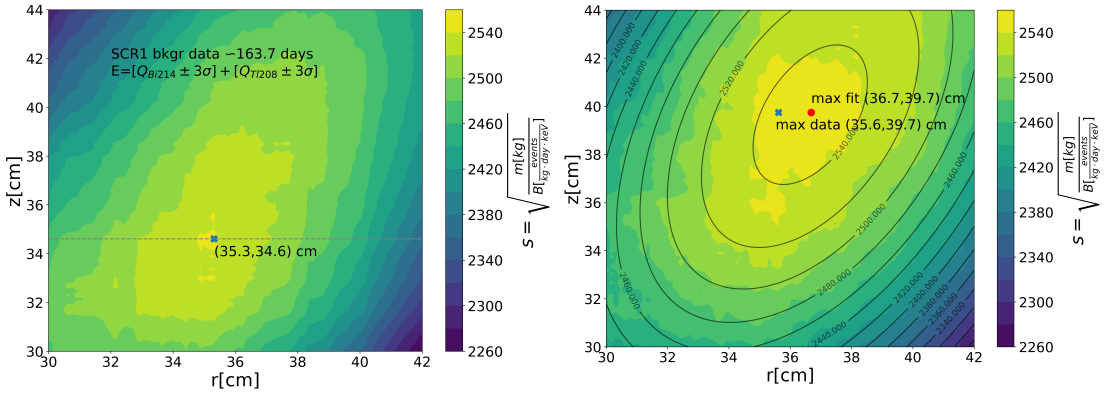

(a) Sensitivity for a cylinder

(b) Sensitivity for $t = 3.5$ including a fit.

Figure 4.4: In (a) the sensitivity evaluated on a two dimensional grid for a cylindrical shape and in (b) the same for a shape with $t = 3.5$, including a quadratic fit and the maximal point.

To be able the compare the found values, a one dimensional projection on the fiducial mass through the maximum was created, see figure 4.5. The highest sensitivity is reached by using neither a cylindrical nor an ellipsoidal shape but an edgy superellipsoid with $t = 3.5$. In order to not pick up a result that is heavily affected by statistical fluctuations the optimal dimensions were selected as the maximum of a two dimensional quadratic fit to the contour lines of the sensitivity, see figure 4.4 (b).

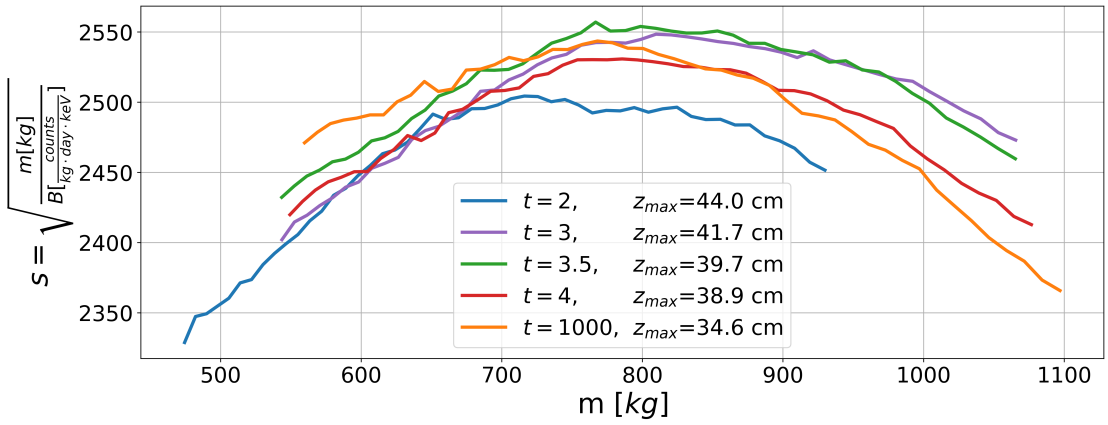

Figure 4.5: Sensitivity curves through the maximal values of each 2D contour plot. The x-axis is converted to mass with equation 4.4.

The results of the analysis are summarized in table 4.2 while in figure 4.7 the solution for

energy region 1 is visualized. Constraints in the analysis are only set on the cylindrical symmetry and the origin of the fiducial volume. Of course these constraints could be loosened further by introducing additional free parameters, for example the position of the origin. The higher dimensional optimization should still be manageable but the additional improvement is questionable. The dimensions found through this analysis improve the sensitivity by 1.7% w.r.t to a regular ellipsoid, that previously was thought to be the optimal shape. Monte-Carlo simulations for the upcoming Darwin project show similar results for the shape parameter but these are still on going studies.

Energy cut	$r_{opt}[cm]$	$z_{opt}[cm]$	$t_{opt}[-]$	mass $[kg]$
1) Bi241 and Tl208 peaks	36.7 ± 0.5	39.7 ± 0.7	3.5 ± 0.5	812 ± 37
2) Full range - blinded region	36.5 ± 0.4	39.4 ± 0.7	3.5 ± 0.5	796 ± 32

Table 4.2: Results for the fiducial volume in the two regions considered. The error calculus is moved to appendix 6.3.

The definition of the energy region is the most crucial part in this analysis. This selects the distribution of events, the total rate and the increase of the rate towards the walls of the TPC. Since the sum of the two cobalt lines at 1.1 and 1.3 MeV[7] lies in the region of interest, the two lines could be used as an alternative estimation of the expected rate in the blinded region. Applying this definition leads to a much smaller fiducial volume ($m \approx 500kg, t = 3.5$) due to a different spatial distribution of the cobalt events. The cobalt events are coming from construction materials and the rate close to the walls of the TPC is very high compared to the bismuth and the thallium lines. The bismuth and the thallium lines which reflect event coming from an intrinsic source and construction materials, have a similar rate to what is expected for the blinded region. The computed rate[8] in the optimal fiducial volume is approximately $B \approx 1{\cdot}10^{-4} counts/(keV{\cdot}day{\cdot}kg)^{-1}$ which is in agreement with Monte-Carlo simulations for the blinded region, see figure 4.6.

[7]The intermediate state lives for approximately 1 ps.
[8]See appendix 6.2

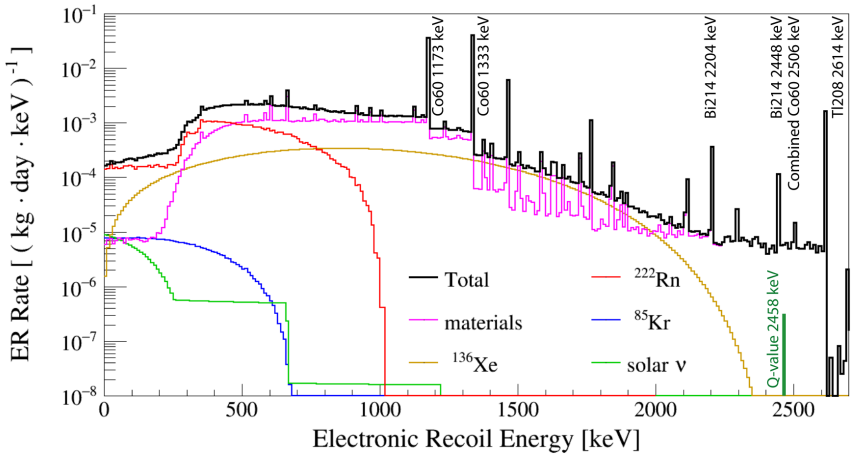

Figure 4.6: Simulated energy spectrum of the total ER background rate in the 1 t fiducial volume (black), and the separate contributions from detector components (purple), 10 μBq/kg of ^{222}Rn (red), 0.2 ppt of ^{85}Kr (blue), solar neutrinos (green) and ^{136}Xe double-beta decay (brown). The spectrum does not include the detector resolution and needs to be smeared with an appropriate resolution function, for example the one from chapter 3. A signal from the $0\nu\beta\beta$ with a half-life of KamLAND-Zen sensitivity of $5.6 \cdot 10^{25}$ years is added. Figure taken and modified from [29].

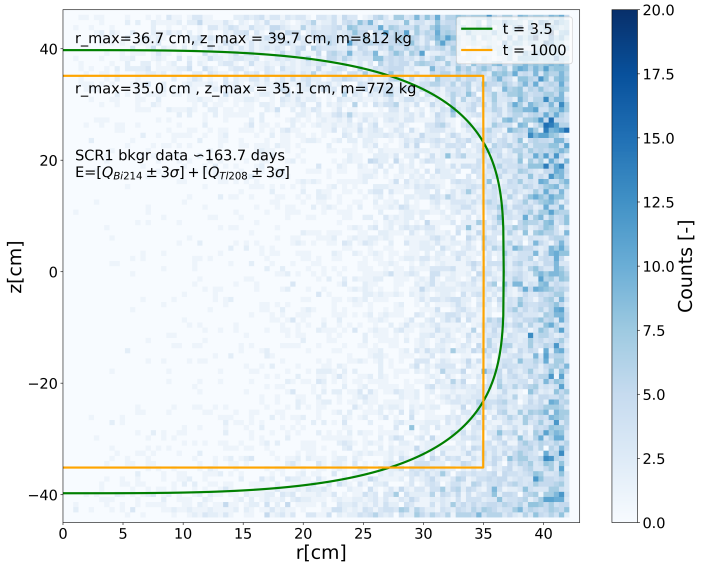

Figure 4.7: Visualization of the fiducial volume analysis results. In green the very best shape (t=3.5) and in yellow the optimal dimensions for a cylindrical shape are shown. It's visible how the green shape avoids events in the corners and get slightly more mass than the cylinder trough a larger height.

Chapter 5

Conclusions and Summary

Table 5.1 summarizes some of the results in the field of research. The values for XENON1T are computed by the author and do not represent the study of the XENON collaboration. The analysis is still ongoing and with increasing efforts and stronger selections better resolutions and background discrimination can be achieved. Due to the measuring time dependence, $S \sim \sqrt{T}$, the sensitivity of XENON1T is expected to increase at least by 23% with respect to the shown value in table 5.1 when the full dataset of 247 days is analysed. The energy resolution and the background rate of the XENON1T experiment are excellent compared to the other xenon experiments, keeping in mind that the experiment was not built for the $0\nu\beta\beta$ search.

Experiment	Isotope & Technique	Exposure $[kg \cdot yrs]$	Resolution at $Q_{\beta\beta}$ [%]	Background $[\frac{counts}{(keV \cdot kg \cdot yrs)}]$	Sensitivity $[10^{24} yrs]$
XENON1T	^{136}Xe, TPC	31	1.1	$\sim 1 \cdot 10^{-4}$	1.9[1]
EXO-200	^{136}Xe, enriched	178	1.2	$\sim 2 \cdot 10^{-3}$	37 [25]
Phase I & II (2018)	single phase TPC				
KamLAND-Zen	^{136}Xe, loaded liquid	504	4.6	$\sim 1 \cdot 10^{-2}$	56 [16]
Phase II (2016)	scintillator				
GERDA	^{76}Ge, diodes	10	0.2	$\sim 1 \cdot 10^{-3}$	40 [30]
Phase I & II (2017)					

Table 5.1: Results and comparison to other experiments. The values for the XENON1T experiment are computed for the derived fiducial volume ($\sim$800kg). Compared to the other enriched experiments the exposure in the XENON1T is relatively low which causes the sensitivity to be lower. The sensitivities are computed with a confidence level of 90 %.

The upcoming XENONnT experiment, which will have a target mass of 5.9 tons, will be able to compete with the current experiments after taking data for a few years and maybe will discover something before the following DARWIN project will look even more

[1] See appendix 6.2 for the computation.

closely for a signal of the hypothetical decay. Figure 5.1 shows the projected empirical sensitivity for the DARWIN and the XENON experiments.

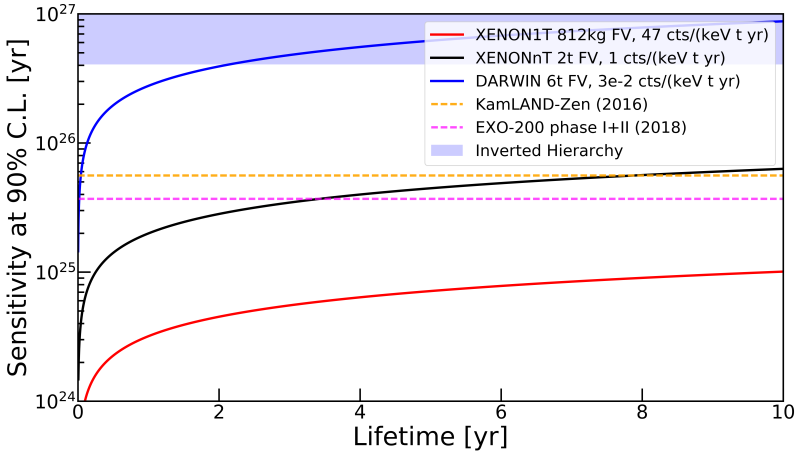

Figure 5.1: The experimental sensitivity for projects related with the XENON and then later with the DARWIN collaborations. DARWIN is expected to reach a competitive half-life sensitivity of 5.6 $\cdot 10^{26}$ years for to the neutrinoless double beta decay after 5 years of data taking [31].

Closing Remarks

Coming back to the problem of unseen planets, which was mentioned to me in the first semester of my physics studies, it is astonishing to see how much more effort has to be made nowadays to increase our knowledge. After Neptune has been postulated in 1846, *M.Galle* had to observe the night sky for about half an hour to find the new planet [1]. With this in mind I want to thank Prof. Dr. Laura Baudis for the chance to see how the current physics questions are tried to be answered and a very special thanks I would like to address to Chiara Capelli who was a great support throughout the project.

Chapter 6

Appendix

6.1 Data Description

Energy Calibration

Pax version: v6.10.1
Background data from science run 1 with a total livetime of 163.7 days.

Applied cuts	Preselection
DAQVeto	cS1 >0
MuonVeto	cS2 >0
S2Threshold	-92.9 < z_{3dnn} < -9 cm
S2Width	r_{3dnn} < 36.94cm
S1SingleScatter	
PosDiff	
S2SingleScatterHE	

Table 6.1: Used cuts and preselections in the energy calibration analysis.

Fiducial Volume Selection

Pax version: v6.10.1 (old LCE maps)
Background data from science run 1 with a total livetime of 163.7 days.

Applied cuts	Preselection
DAQVeto	cS1 >0
MuonVeto	cS2 >0
S2Threshold	-95 < z_{3dnn} < -5 cm
S2Width	r_{3dnn} < 42cm
S1SingleScatter	
PosDiff	
S2SingleScatterHE	

Table 6.2: Used cuts and preselections in the fiducial volume analysis

6.2 Sensitivity and Rate Computations

Sensitivity:

$$S = \frac{ln(2) \cdot \varepsilon \cdot \eta}{n_\sigma \cdot \mathcal{M}_A} \sqrt{\frac{T}{\Delta E}} \sqrt{\frac{M}{B}}$$

$$= \frac{ln(2) \cdot 0.9 \cdot 0.0849}{1.6 \cdot 2.25 \cdot 10^{-25} kg} \sqrt{\frac{163.7 days}{2.35 \cdot 0.011 \cdot 2458 keV}} \cdot 2550 kg \sqrt{keV \cdot days} \frac{1}{365 \frac{days}{year}}$$

$$= 1.93 \cdot 10^{24} years$$

Normalized Background Rates

Energy region 1: $E = [Q_{Bi214} \pm 3\sigma] + [Q_{Tl208} \pm 3\sigma]$

Energy region 2: $E = [Q_{Bi214} - 3\sigma, Q_{Tl208} + 3\sigma] - \underbrace{Q_{\beta\beta} \pm 4\sigma}_{blinded\ \ region}$

Volume	Counts $[-]$	Mass $[kg]$	Time $[days]$	Energy $[keV]$	Energy Region	Rate $[\frac{10^{-4}}{keV \cdot day \cdot kg}]$
total dataset	16337	2853	163.7	289.1	1	1.2
optimal FDV	5069	812	163.7	289.1	1	1.3
total dataset	17499	2853	163.7	407.6	2	0.91
optimal FDV	4884	796	163.7	407.6	2	0.92

Table 6.3: Computation of background rates for different volumes and the two selected energy regions.

Volume	Counts$[-]$	Mass$[kg]$	Time$[days]$	Energy$[keV]$	Rate$[\frac{10^{-4}}{keV \cdot day \cdot kg}]$
total dataset	210440	2853	163.7	150	29
optimal FDV	15329	514	163.7	150	12

Table 6.4: Computation of background rates for the two cobalt lines.

Cobalt lines energy cut:
$E = [Q_{Co60-1173MeV} \pm 3\sigma] + [Q_{Co60-1333MeV} \pm 3\sigma]$ with $\sigma = 1\%$

FDV:
$r_{opt} = 32.7cm \qquad z_{opt} = 31.5cm \qquad t_{opt} = 3.5 \qquad m = 514kg$

6.3 Fiducial Volume Error Calculus

Standard error on fit values

Assuming there is an standard error ϵ_i (computed by the fitting algorithm) on each parameters a_i of the quadratic fit function $f(r, z, a_i)$, it's easy to compute a shift in the maximum by computing the maximum of $f(r, z, a_i + \epsilon_i)$ and $f(r, z, a_i - \epsilon_i)$.

This leads to:
$r_{max} = 36.7 \pm 0.5cm$
$z_{max} = 39.7 \pm 0.7cm$
With these values the error in the mass is compute to be: $m = 812 \pm 37kg$

Krypton

Since the krypton produces very uniformly distributed events within the TPC, on can estimate the error on the mass of the fiducial volume m_FD by using the following ratio.

$$\frac{m_{FD}}{m_{total}} = \frac{Counts_{FD}}{Counts_{total}} \quad \longrightarrow \quad m_{FD} = m_{total} * \frac{Counts_{FD}}{Counts_{total}} = 883kg \quad \longrightarrow \quad 847.5 \pm 36kg$$

m_{total}: Total mass of selected data.
$Counts_{total}$: Total number events of the selected dataset.

This method reveals an unexpectedly big uncertainty which lead to doubt about the validity of the method. Plotting the radial and height dependence of the right- and lefthandside of above ration indeed shows a small discrepancy. Due to the discrepancy the error was taken as the result of the previous computation, the uncertainty through the standard error on the fit values.

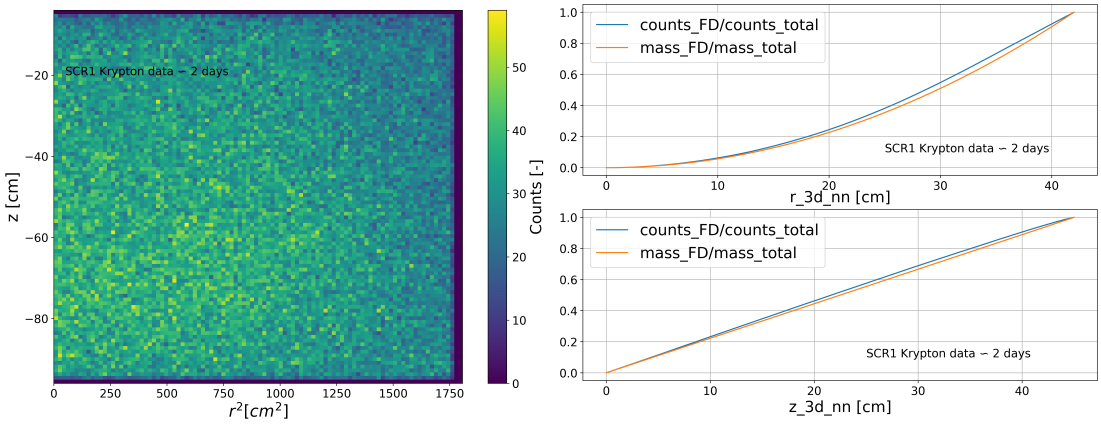

(a) Uniformly distributed krypton events

(b) radial and height dependence of the ratio

Figure 6.1: Krypton event distribution and the ratios coordinate dependence.

Applied cuts	Preselection
S2Threshold	r_3d_nn < 42cm
S2Width	-95 < z_3d_nn < -5 cm
3 < ds_s1_b_n_distinct_channels < 30	
600 < (s1_b_center_time-s1_a_center_time) <2000	
s2_a > 1000	
150 < cs1_a < 350	
25 < cs1_b < 160	

Table 6.5: Krypton data selection

Bibliography

[1] Charles Kittel et al. *Mechanik*. Berklek Physik Kurs 1. 1991, p. 105. ISBN: 3-528-48351-2.

[2] Vera C. Rubin, W. Kent, and Jr. Ford. "Rotation of the Andromeda Nebula from a Spectroscopic Survey of Emission Regions". In: *The Astrophysical Journal* 159 (Feb. 1970), p. 379. DOI: 10.1086/150317.

[3] Milkyway@home. *How do we Search for Dark Matter?* Ed. by Matthew Newby. 2019. URL: https://milkyway.cs.rpi.edu/milkyway/science.php.

[4] Douglas Clowe et al. "A Direct Empirical Proof of the Existence of Dark Matter". In: *The Astrophysical Journal* 648.2 (Aug. 2006), pp. L109–L113. DOI: 10.1086/508162.

[5] Chandra X-ray Observatory. *1E 0657-56: NASA Finds Direct Proof of Dark Matter*. Ed. by X-ray: NASA/CXC/CfA/M.Markevitch et al.; Optical: NASA/STScI; Magellan/U.Arizona/D.Clowe et al.; Lensing Map: NASA/STScI; ESO WFI; Magellan/U.Arizona/D.Clowe et al. 2006. URL: http://chandra.harvard.edu/photo/2006/1e0657/.

[6] Volker Springel, Carlos S. Frenk, and Simon D. M. White. "The large-scale structure of the Universe". In: *Nature* 440.7088 (Apr. 2006), pp. 1137–1144. DOI: 10.1038/nature04805.

[7] Prasenjit Saha and Paul A. Taylor. *The Astronomers' Magic Envelope*. Oxford University Press, June 6, 2018. DOI: 10.1093/oso/9780198816461.001.0001.

[8] E. Aprile et al. (XENON Collaboration). "The XENON1T dark matter experiment". In: *The European Physical Journal C* 77.12 (Dec. 2017). DOI: 10.1140/epjc/s10052-017-5326-3.

[9] Erik Hogenbirk. "A spark in the dark , Scintillation time dependence and neutron-induced signals in dual-phase xenon TPCs". PhD thesis. Universiteit van Amsterdam, 2019.

[10] E. Aprile et al. (XENON Collaboration). "Dark Matter Search Results from a One Ton-Year Exposure of XENON1T". In: *Physical Review Letters* 121.11 (Sept. 2018). DOI: 10.1103/PhysRevLett.121.111302.

[11] Thomas Gehrmann, Vincenzo Chiochia, and Günther Dissertori, eds. *Phenomenology of Particle Physics Script*. 2010.

[12] Mark Thomson and Nico Serra. *Kern- und Teilchenphysik II, Lecture 10: Deep Inelastic Neutrino Scattering*. 2018. URL: https://www.physik.uzh.ch/de/lehre/PHY213/FS2018.html.

[13] E. Aprile et al. (XENON Collaboration). "Observation of two-neutrino double electron capture in 124Xe with XENON1T". In: *Nature* 568.7753 (Apr. 2019), pp. 532–535. DOI: 10.1038/s41586-019-1124-4.

[14] Stefano Dell'Oro et al. "Neutrinoless Double Beta Decay: 2015 Review". In: *Advances in High Energy Physics* 2016 (2016), pp. 1–37. DOI: 10.1155/2016/2162659.

[15] K. H. Ackermann et al. (GERDA Collaboration). "The Gerda experiment for the search of $0\nu\beta\beta$ decay in 76Ge". In: *The European Physical Journal C* 73.3 (Mar. 2013). DOI: https://doi.org/10.1140/epjc/s10052-013-2330-0.

[16] A. Gando et al. (KamLAND-Zen Collaboration). "Search for Majorana Neutrinos Near the Inverted Mass Hierarchy Region with KamLAND-Zen". In: *Physical Review Letters* 117.8 (Aug. 2016). DOI: 10.1103/PhysRevLett.117.082503.

[17] J. B. Albert et al. (EXO Collaboration). "Search for Majorana neutrinos with the first two years of EXO-200 data". In: *Nature* 510.7504 (June 2014), pp. 229–234. DOI: https://doi.org/10.1038/nature13432.

[18] A. Gando et al. (KamLAND-Zen Collaboration). "Limit on Neutrinoless$\beta\beta$ Decay of Xe136from the First Phase of KamLAND-Zen and Comparison with the Positive Claim in Ge76". In: *Physical Review Letters* 110.6 (Feb. 2013). DOI: https://doi.org/10.1103/PhysRevLett.110.062502.

[19] Carl Eric Dahl. "The physics of background discrimination in liquid xenon, and first results from Xenon10 in the hunt for WIMP dark matter". PhD thesis. Princeton U., 2009. URL: https://www.princeton.edu/physics/graduate-program/theses/theses-from-2009/E.Dahlthesis.pdf.

[20] Jelle Aalbers. "Dark Matter Search with XENON1T". PhD thesis. Institute for High Energy Physics (IHEF), June 19, 2018.

[21] P. T. Boggs and J. E. Rogers. "Orthogonal distance regression". In: (1989). DOI: 10.6028/nist.ir.89-4197.

[22] SciPy.org. *Orthogonal distance regression*. Ed. by The SciPy community. Aug. 17, 2019. URL: https://docs.scipy.org/doc/scipy/reference/odr.html.

[23] Glenn F.Knoll. *Radiation Detection and Measurement*. 2000.

[24] P. M. McCowan and R. C. Barber. "Qvalue for the double-beta decay of Xe-136". In: *Physical Review C* 82.2 (Aug. 2010). DOI: 10.1103/PhysRevC.82.024603.

[25] J. B. Albert et al. (EXO-200 Collaboration). "Search for Neutrinoless Double-Beta Decay with the Upgraded EXO-200 Detector". In: *Physical Review Letters* 120.7 (Feb. 2018). DOI: 10.1103/PhysRevLett.120.072701.

[26] SciPy.org. *Numpy Histogram Bin Edges*. Ed. by The SciPy community. Jan. 31, 2019. URL: https://docs.scipy.org/doc/numpy/reference/generated/numpy.histogram_bin_edges.html#numpy.histogram_bin_edges.

[27] J. J. Gómez-Cadenas and J. Martin-Albo. "Phenomenology of neutrinoless double beta decay". In: (July 2015). DOI: 10.22323/1.229.0004. URL: https://pos.sissa.it/cgi-bin/reader/conf.cgi?confid=229.

[28] Superellipsoid. *Superellipsoid — Wikipedia, The Free Encyclopedia*. [Online; accessed 11-Juli-2019]. 2019. URL: https://en.wikipedia.org/wiki/Superellipsoid.

[29] E. Aprile et al. (XENON Collaboration). "Physics reach of the XENON1T dark matter experiment." In: *Journal of Cosmology and Astroparticle Physics* 2016.04 (Apr. 2016), pp. 027–027. DOI: 10.1088/1475-7516/2016/04/027.

[30] M Agostini et al. "First results from GERDA Phase II". In: *Journal of Physics: Conference Series* 888 (Sept. 2017), p. 012030. DOI: 10.1088/1742-6596/888/1/012030.

[31] L. Baudis et al. "Neutrino physics with multi-ton scale liquid xenon detectors". In: *Journal of Cosmology and Astroparticle Physics* 2014.01 (Jan. 2014), pp. 044–044. DOI: 10.1088/1475-7516/2014/01/044.